Chapter 6

Analysis of Contact Instability in the Virtual Wall

6.1 Introduction

With the new virtual wall controllers of Chapter 5 in hand, we are ready to make a purchase. Our controllers may be used to buy improved performance for virtual walls —at the expense of a slightly increased computational burden [1]. But before we can judge the prudence of our purchase, we would like to know what our virtual walls stand to gain. Just how much performance improvement may a virtual wall designer expect to enjoy after having paid the price of controller design according to Chapter 5? How bad were the destabilizing effects of the ZOH and the intersample threshold crossing (ITC) in the first place? Our goal for the present chapter, motivated by these questions, is to find measures for the performance improvements afforded by the virtual wall controllers developed in the previous chapter.

As discussed in the introduction to Chapter 5, the problem appears to be a serious one if we are

[1] The increase in computational burden which the controllers of chapter 5 represent (the price to be paid) deserves careful evaluation—it is actually quite small. The zero order hold (ZOH) effect-compensating controller of section 5.4.2 (pole-placement design) requires no extra run-time computation over the standard virtual wall controller —its structure is identical to the standard damped wall controller, only the gain settings are different. To compensate for the ZOH using the half-sample prediction algorithm of section 5.4.1, a certain amount of computational overhead is added at each sampling step. Most of the computations associated with the dead-beat control technique of sections 5.4.3, used to compensate for inter-sample threshold crossing (ITC) may be spread out among the steps within the wall, so that their computational impact is also small.

These new controllers do of course require extra off-line analysis and the execution of a system identification experiment to produce the human impedance model, but these costs do not need to be factored into measures of run-time computational complexity. To locate computations off-line is quite desirable from an engineering viewpoint —delegation is always appropriate when resources are tight.

to judge by the number of virtual wall explorers who have noticed, and researchers who have reported the phenomenon of contact instability. Most every virtual wall designer encounters contact instability as he or she turns up the gain, attempting to create a stiff wall—or turns down the sample rate, attempting to create a computationally efficient wall [2]. Undeniably, contact instability associated with virtual walls remains a serious impediment to further development of virtual environments. It limits the palette of objects which may be placed inside a believable virtual environment.

But we would prefer to judge the magnitude of the problem of contact instability by a quantitative measure other than popular vote. For a gauge of the contact stability problem associated with a particular virtual wall controller, I propose the use of the smallest inherent viscous damping which must be present in the human and/or manipulandum to just guarantee system stability (where the *system* is made up of the human, manipulandum, and virtual wall controller). A finite amount of damping will be required to guarantee system stability of 'standard' virtual walls to compensate for the destabilizing effects of the ZOH and intersample threshold crossing. By contrast, no damping will be required to guarantee system stability for the virtual walls implemented with the controllers of chapter 5, since these controllers, by design, do not suffer the destabilizing effects of the ZOH and intersample threshold crossing. Thus the stabilizing damping coefficients to be associated with the old controllers may be regarded as measures for the performance improvements offered by the new controllers.

Our present task, then, is to size stabilizing damping coefficients. Since the destabilizing effects under scrutiny may be viewed as pathways for the flow of energy into the system, we may equivalently interpret our task as the regulation of the rate of energy dissipation. Note that with the choice of viscous damping for dissipation, we restrict the dissipation rate to be proportional to velocity squared, which may not be the case for the rate of energy introduction. Thus we will have to be cognizant about the degree to which our measure is conservative. Linear damping may not always be the least conservative measure of non-linear energy-introduction.

One caveat remains before launching into a search for damping coefficients. If the zero-order hold effects have already been taken care of, the intersample threshold crossing may either introduce energy or *extract* energy. At wall entry it introduces, at wall exit it extracts. We may expect the two effects to balance—but we cannot prove this supposition without a full analysis. [3] For

[2] Naturally, virtual wall algorithms which can tolerate long sampling periods are highly valued because they allow the comparatively modest computing resources of the computers with which virtual haptic environments are typically implemented (personal computers) to be spent on other time-critical tasks such as graphic updates or networking. Note that personal computers support the hardware interfacing needs of haptic display whereas more powerful computers usually do not

[3] The proof that the energy introduced is balanced by energy extracted will not be undertaken in this chapter. We will stop short of this goal because our problem turns out to be extremely complex. Similar but more tractable problems which have been treated in the field of nonlinear dynamics will be discussed to tentatively infer that a bound on the net energy introduced does in fact *not* exist. In this chapter, we will instead concentrate on *worst-case*

the purposes of finding a measure for the destabilizing effects of intersample threshold crossing, we choose the damping coefficient which will balance the *worst-case* energy introduction. We seek the energy dissipation rate which will balance energy introduced by a full sampling period's delay in turning on and no delay in turning off the wall controller.

For the present, we shall assume that the virtual wall controller is designed to render a wall without virtual damping and that the only means of energy dissipation (aside from the discontinuity in constraint) is through an inherent damper. In this manner we may consider the inherent damping coefficient to be sized for the manipulandum a measure of the destabilizing effects of the discretely implemented virtual wall controller. Extensions to our methods for finding the stabilizing damping coefficient when the virtual wall contains damping will be discussed in the conclusion to this chapter. We will further chose to deal with models of all participants (human, manipulandum, and controller) which are linear except for the discontinuity of the switching wall controller. The behavior we look for when the damper is properly sized (when the energy introduction is perfectly balanced by dissipation is sustained oscillations, indicative of marginal stability. Note that sensitivity to initial conditions wll have to be checked since the energy dissipation rate will certainly be path-dependent, and the energy introduction may be path-dependent in a different manner.

6.1.1 Passivity versus Stability

The answer to the above damper sizing task can only be given with reference to a particular system or at best, class of systems. Yet one participant in the system will always defy modeling and characterization: the human. At issue is just how we will model the human for purposes of analysis, or how we will restrict the set of behaviors which the human may exhibit within our assumed system. We cannot leave the human out of the analysis, since uncoupled stability is not what we are interested in. Indeed, the human finger plays a significant role in determining the stability of this coupled system. Given that the human is capable of many roles, including active behavior, and that as 'audience' or virtual wall explorer, the human should ideally be left free of restrictions or constraining models, it must be acknowledged that our analysis task is quite difficult.

However, as discussed in the previous chapter, virtual wall contact instability is observed without volitional control on the part of the human, that is, when the human can be modeled as an impedance and a bias force. In the interest of minimally restricting the human, in fact to essentially treat the virtual wall and manipulandum without explicit reference to the human impedance, yet guarantee *system* stability, Colgate has called upon the passivity theorem in his recent work [24] and [21]. By assuming that the human remains passive, stability of the *coupled* system may be guaranteed

---

assumptions.

simply by restricting the *uncoupled* controlled manipulandum to remain strictly passive. For the passivity theorem states that the coupling of a passive and a strictly passive system creates a system which will remain stable. An inherent damper can be sized for the manipulandum which will restrict its controlled behavior to that of a strictly passive system, and this damper may be sized without reference to the human impedance. That is, the expression for the lower bound on the inherent damping will not contain any assumed mechanical properties for the human. Auspiciously, this certain inherent damping will guarantee absence of contact instability no matter what human comes up to explore the virtual wall, so long as that human takes on a linear time-invariant (LTI) passive impedance. Colgate's results based on the passivity theorem and their implications for design have proven quite valuable and will be further discussed in the literature review below.

However, Colgate's lower bound on inherent damping to guarantee passivity, which only restricts the human to the class of all LTI passive operators, is not quite pertinent as a measure for the performance improvement offered by our controllers. Our controller designs make use of much more restrictive assumptions about the role of the human in the system. We model the human as a *particular* second order impedance, and make use of that model within the controller for prediction. Having adopted the viewpoint that the human can be modeled by a particular impedance, and even folding in the idea of an on-line system identification experiment (to characterize that impedance) into the controller design, Colgate's results based on less restrictive assumptions may be considered conservative for our purposes. We are therefore interested in lower bounds for the inherent damping which stabilize a system which includes a *particular* human impedance. In seeking these bounds, we are (once again) considering a problem of stability rather than passivity, and in our presentation of lower bounds, we will be required to make reference to the assumed human impedance.

6.1.2 Outline

In this chapter, we will treat the destabilizing effects of the ZOH and intersample threshold crossing independently. Although we cannot rely on the superposition of the two effects given that we are dealing with a nonlinear system, we are nevertheless interested in separate measures. We would like a measure of the destabilizing effects of the ZOH alone, since we may choose to implement a new controller with ZOH-compensation, but without ITC compensation. Adding the damping coefficient given as a measure of the ITC destabilizing effects to a ZOH-alone compensating controller would account for the ITC effects and thereby guarantee stability. We also undertake the two issues separately in the interest of simplicity of analysis.

The remainder of this chapter is divided into three main sections. Section 6.1 reviews the literature with regard to stability measures for nonlinear systems such as ours. Section 6.2 analyzes

the destabilizing effects of the ZOH on certain models. Section 6.3 treats the destabilizing effect of the intersample threshold crossing. Finally, section 6.4 wraps up.

6.2 Literature Review

The use of a smallest damping coefficient as a measure of the destabilizing effects in a system is by no means new. To alter a system with the addition of damping (inherent or virtual) is a natural and reliable means of stabilizing a linear system —it is a standard tool of the controls engineer when a destabilizing effect cannot otherwise be removed. Our choice of viscous damping as a measure of *nonlinear* destabilizing effects is perhaps unique, but probably not to be celebrated, as it is may not be reliable. No claims as to originality or extensibility are being made about the stabilizing damping coefficients found in this chapter. Their intended use, as discussed in the introduction, is for measuring the size of a problem—a problem for which we already have a solution. Basically, these damping coefficients are derived to lend support to statements of usefulness about our solution to the contact instability problem —the new controllers of Chapter 5.

Interestingly, though, Chapter 5 (and by association the present chapter) represent in some significant ways a departure from recent work on the virtual wall. Our contributions to the contact instability problem are new controller designs, whereas most recent work has been centered on analytical treatments of the standard virtual wall controller yielding design guidelines pertaining only to the standard controller. Rather than building on recent analytical results, we have chosen to reject the standard controller and start from scratch on the design problem. Since we now have controllers in hand which are not subject to the energy-introducing effects of the sampled data implementation, we are no longer interested in design guidelines regarding sampled data energetics. Our new designs instead inspire us to undertake some modified analytical treatments of the standard virtual wall. In particular, because our controllers make certain assumptions which were not a part of recent analytical work, we are compelled to revisit this analytical work, incorporate our assumptions, and thereby adapt it for our purposes.

In preparation for the analytical treatments of this chapter, I will give a rather complete review of Colgate's passivity analysis. The subtleties between the results presented here and those presented by Colgate have to do with assumptions of the role of the human in the system (and controller design). The implications of these assumptions lie in degree of conservativeness of results.

A further purpose for covering the literature in such detail is to highlight the one attribute of the standard virtual wall controller which has not been treated explicitly in any published work: the effect of intersample threshold crossing.

6.2.1 Passivity Analysis

Our controllers are designed to work with a particular human impedance, and, when implemented in full, will render stable walls without requiring any extra stabilizing damping from the manipulandum or human. This being the case, the lower bound on inherent manipulandum damping to guarantee passivity determined analytically by Colgate is not quite appropriate as a measure for the performance improvement offered by our new controllers. Rather than incorporating a particular assumed human impedance, Colgate's analyses assumed that the human impedance simply belongs to a class of impedances —the class of all LTI passive impedances. We are now looking for instability measures consistent with the spirit of our new controller designs, that is, which make particular assumptions about the human impedance. We shall be deriving such measures (pertaining to the ZOH effects) with linear stability analyses in the discrete domain.

A comment regarding Colgate's passivity treatment is in order, however. There lies a power in the passivity formalism which makes the results particularly amenable for use as design guidelines. That is, that the damping coefficient which guarantees passivity may be expressed in terms of the transfer function of the controller alone; the human impedance properties are not part of the expression. Our analyses in this chapter, precisely because of our desire to incorporate a particular human impedance, will not take advantage of this power.

Colgate's derivation of the passivity condition for sampled data systems is presented in [24]. Colgate's result is expressed as a lower bound on inherent damping, is based (as is the proof of the passivity theorem) on the small gain theorem. Because the small gain theorem takes only magnitude information into account and completely disregards phase, linear fractional transformations (which have equivalent interpretations as loop transformations and coordinate changes) must be used to reduce conservativeness in applications of the small gain theorem. Using only the constraint that the human operator be passive, Colgate first finds the area in the Nyquist plane within which a passive human operator in feedback connection with the manipulandum and linked with a zero-order hold and integrator must lie. This area (a disk) can be mapped to the unit disk (uncertain phase; unity magnitude) by a linear fractional transformation (LFT). A corresponding LFT (coordinate transform) is found for the discrete controller in [21]. Placing the unit disk as a constraint upon this area in the Nyquist plane to which the controller is mapped by this LFT then guarantees coupled stability by the small gain theorem.

A statement of sufficiency is derived via an observation regarding stored kinetic energy. By requiring that the kinetic energy of the mass of the manipulandum never be as great as the total energy input by the human source, the same lower bound on inherent damping is derived as in the necessary condition except that there appears a modulus around the transfer function of the

controller.

Colgate's analysis as outlined thus far does not account for the unilateral nonlinearity of the virtual wall. In fact, all components have been assumed linear up to this point. Colgate extends the sufficiency statement to cover a switching controller by making the observation that, since without its feedback controller the manipulandum is passive, if the control input (from the actuator) is set to zero (turned off) at any time, passivity properties will not be affected. This statement does not, however, account for the possible introduction of a small amount of potential energy when the controller is turned *on*. Due to the possibility of crossing the threshold between sampling times, up to a full sampling period T may have elapsed before the wall control law is enacted and the wall will, upon being turned on, effectively hold potential energy without having had the requisite work done on it.

In this chapter we will treat the effects of intersample threshold crossing explicitly.

In an altogether different approach to the contact instability problem, Tsai and Colgate treat the unilateral nonlinearity explicitly in [95]. This analysis, in contrast to that of [24] and [21] is made entirely in the discrete domain. A zero-order-hold equivalent of the plant in feedback connection with a assumed human impedance is found, and used together with a result in filter theory having to do with the saturation non-linearity by Mitra [75].

Rather than via a circle criterion, which uses sector bounds, more complete information about the unilateral nonlinearity is exploited. Tsai and Colgate's results are presented as a Nyquist domain criterion which is reminiscent of the circle criterion. Rather than circles, the forbidden zone for the Nyquist plot of the controller becomes a wedge whose size is frequency-dependent.

In our treatment of the energetics of the intersample threshold crossing, we shall be making use of Poincaré maps—a standard tool in the field of nonlinear dynamics. Although we shall not be contributing to this field, nor making direct use of any theorems from it, I will briefly review similar applications of Poincaré maps and associated stability theorems, especially in the field of robotics.

In the field of robotics, Poincaré maps have been utilized by Koditscheck and Bühler in [17] and [16] to investigate the existence and stability of limit cycles in Raibert's hopping robots and in juggling robots in their own lab. Using some reasonable assumptions regarding the map relating the strike time and strike velocity from one hop to the next can be shown to be one-dimensional. The fact that the map is one dimensional is in fact quite fortuitous— many graphical techniques and related theorems may then be applied. Unfortunately the maps we shall encounter in this chapter having to do with sustained oscillations fed by intersample threshold crossing are two-dimensional and extremely complicated. We shall be making several simplifying assumptions.

Holmes and x have treated the dynamics of a bouncing ball in [47]. Also documented in the popular book by [37]. Their system involved a ball bouncing with a coefficient of restitution on a table which vibrates vertically with a sinusoidal motion. Whether the ball strikes the table in its upward or downward motion is a function of the time spent in the air (an undamped gravity field) which in turn is a function of the last strike time and velocity. As it turns out, this two-dimensional map also reduces to a one-dimensional map. Its dynamics are quite complex, however. Holmes shows the existence of a cascade of period-doubling bifurcations of the limit cycle leading to chaos as the parameters are varied.

Budd and Dux treat a similar system in [15]. But rather than a ball bouncing on a vibrating table, they treat a sprung mass striking a stationary wall where the spring anchor is driven sinusoidally. Theirs is primarily a numerical study.

6.3 Effects of the Sample and Hold

In this section I will develop a measure for the destabilizing influence of the sample and hold operator in our system. The next section will treat the effects of intersample-threshold crossing.

We are interested in sizing an inherent damper within the manipulandum which will guarantee stability when a particular impedance (the human) is coupled, and the virtual wall is simply a spring. We will answer this question with a treatment in the discrete domain. Specifically, a zero-order hold equivalent will be found for the model of the manipulandum together with the human and a linear discrete stability analysis will reveal the damping coefficients.

6.3.1 Uncoupled Stability

Before beginning with the coupled stability analysis, we look at uncoupled stability, in part to outline the procedure.

Our model for the manipulandum is:

$$G(s) = \frac{1}{s^2(ms+b)} = \frac{1}{b}\frac{a}{s^2(s+a)} \tag{6.1}$$

where

$$a = b/m \tag{6.2}$$

The zero-hold equivalent is readily found using a table of Z-transforms, for example, from [31]:

$$G_{zoh}(z) = \frac{1}{b}\frac{z-1}{z}\mathcal{Z}\left\{\frac{G(s)}{s}\right\} = \frac{1}{b}\frac{(aT-1+e^{-aT})z + (1-e^{-aT}-aTe^{-aT})}{a(z-1)(z-e^{-aT})} \tag{6.3}$$

Parameter Values for Figure 6.2

Parameter		Value	Units
m	=	0.30	kg
k	=	500	N/m

In feedback connection with a controller $H(z) = K$, as in Figure 6.1, our closed loop characteristic equation becomes:

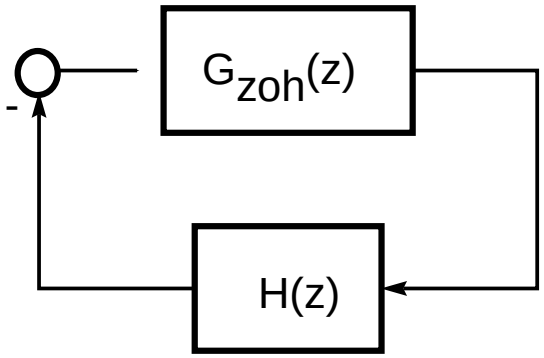

Figure 6.1: *Feedback connection between manipulandum and controller, no human impedance coupled*

$$z^2 + \left[\frac{K}{ab}aT - (\frac{K}{ab} + 1) + (\frac{K}{ab} - 1)e^{-aT}\right] z + \left[\frac{K}{ab} - (\frac{K}{ab} - 1)e^{-aT} - \frac{K}{ab}aTe^{-aT}\right] = 0 \qquad (6.4)$$

We seek the values of b which place the roots of the characteristic equation on the unit circle. These may be found by setting the last term of the previous equation equal to unity.

This produces the equation:

$$e^{-bT/m}\left[1 - \frac{KT/b}{(1 - mK/b^2)}\right] = 1 \qquad (6.5)$$

The damping coefficients which produce marginal stability may be found numerically and plotted as a function of the sampling period, as in Figure 6.2. Values have been assumed for each of the parameters in producing this plot, as shown in Table 6.3.1

The results for uncoupled stability may be presented in non-dimensional parameters as suggested

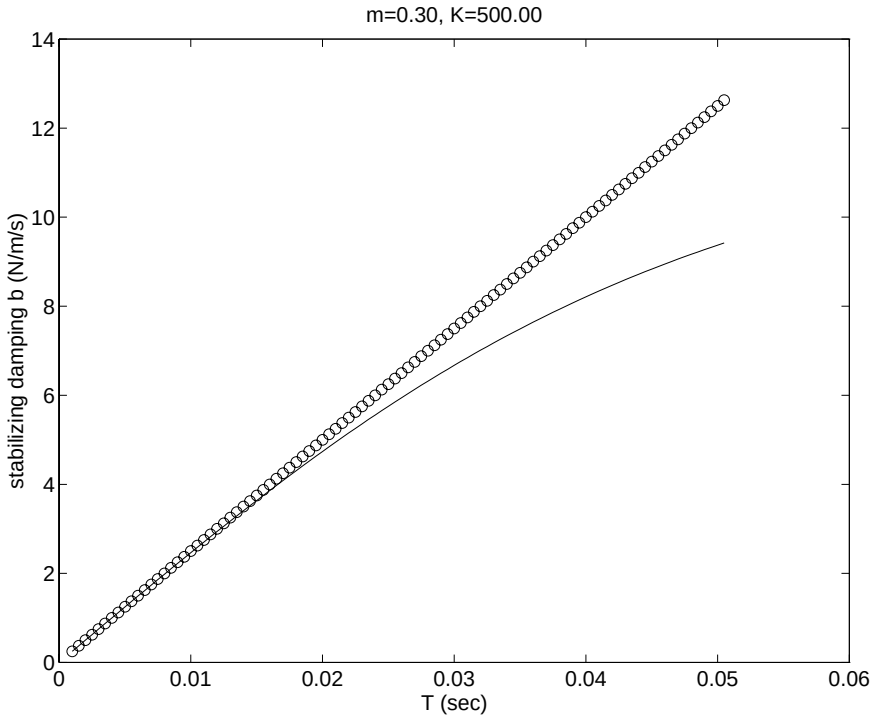

Figure 6.2: *Stabilizing Damping versus Sampling Period*

by Colgate (See [24]):

$$\tau = bT/m \quad \alpha = kT/b \tag{6.6}$$

Equation 6.5 reads, in non-dimensionalized parameters:

$$e^{1/\tau} = 1 - \frac{\alpha}{1 - \tau\alpha} \tag{6.7}$$

We may plot this alongside the passivity region derived by Colgate in a graph of α versus τ, which has been done in Figure 6.3. Note that the parameter space for uncoupled stability is larger than that for passivity.

A simulation may be used to check marginal stability of a borderline damping coefficient. Selection of the point circled in Figures 6.2 and 6.3, for example, produces marginal stability as expected: See Figure 6.4.

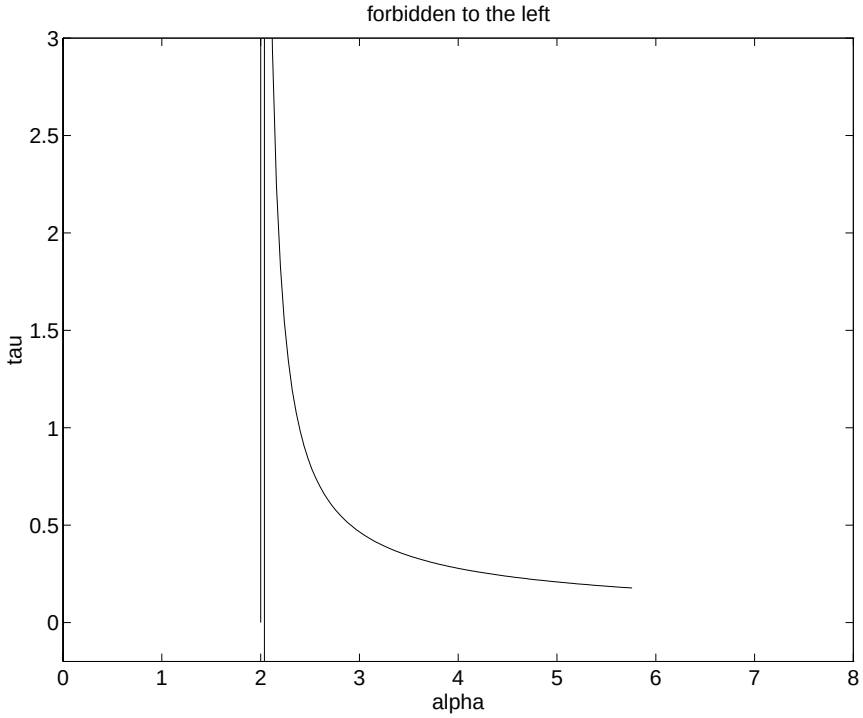

Figure 6.3: *Alpha versus Tau*

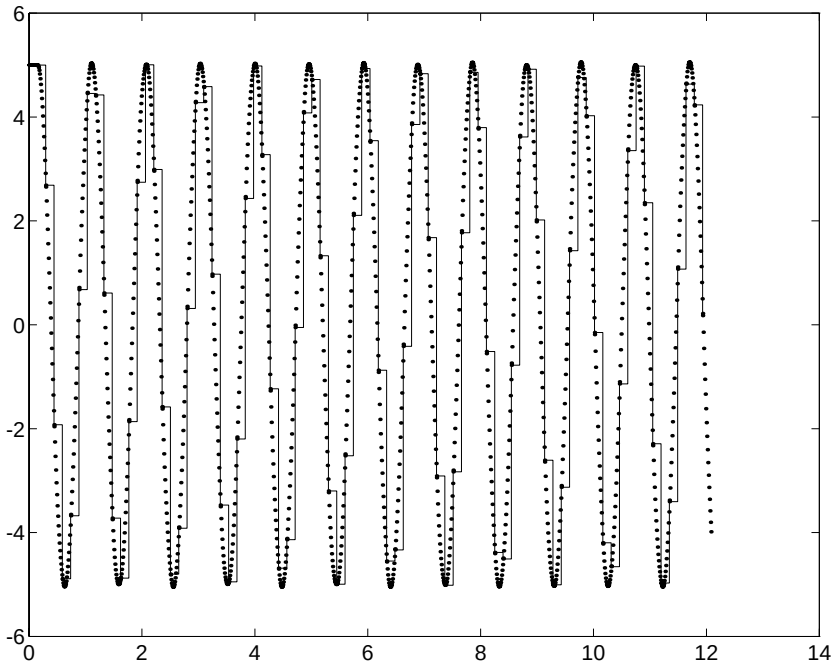

Figure 6.4: *Verification of marginal stability by simulation*

6.3.2 Coupled Stability

To treat stability when the manipulandum is coupled to a particular impedance, we may follow the same basic procedure after making a reasonable assumption about the manner in which the human impedance is coupled to the manipulandum. We shall assume that the mechanical coupling between the effective mass of a human finger and the mass of the manipulandum is direct, as shown in Figure 6.5. We neglect the compliance of the fingertip skin in making this assumption. These assumptions are consistent, however, with experimental measures of the finger impedance as in the work of Hajian and Howe [39]. Thus the human impedance does not increase the order of our system, and therefore analysis is almost as simple as in the uncoupled case. A block-diagram interpretation of the assumed human impedance/ manipulandum coupling is shown in Figure 6.6

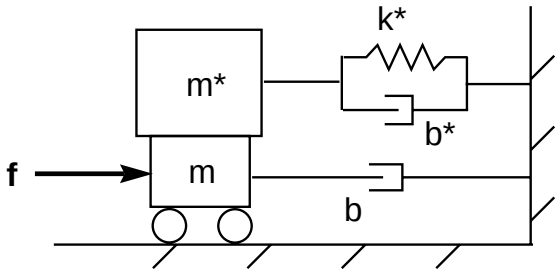

Figure 6.5: *Assumed mechanical coupling between modeled human impedance and manipulandum*

We assume a second order linear impedance to model the human:

$$Z_o(s) = m^* s^2 + b^* s + k^* \tag{6.8}$$

Coupling between the human and manipulandum produces the following expression for the composite impedance:

$$G^*(s) = \frac{1}{(m + m^*)s^2 + (b + b^*)s + k^*} \tag{6.9}$$

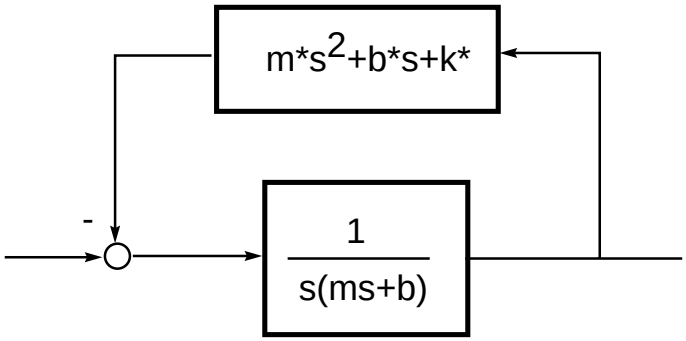

Figure 6.6: *Block diagram interpretation of assumed human-manipulandum mechanical coupling*

The zero order hold equivalent of $G^*(s)$ is:

$$G^*_{zoh}(z) = \frac{1}{k^*}\frac{z-1}{z}\mathcal{Z}\left\{\frac{G^*(s)}{s}\right\} = \frac{1}{k^*}\frac{Az+B}{z^2 - 2e^{-aT}(cosbT)z + e^{-2aT}} \tag{6.10}$$

where

$$\begin{aligned} A &\triangleq 1 - e^{-aT}cosbT - \tfrac{a}{b}e^{-aT}sinbT \\ B &\triangleq e^{-2aT} + \tfrac{a}{b}e^{-aT}sinbT - e^{aT}cosbT \end{aligned} \tag{6.11}$$

A feedback connection between this transfer function and the simple controller $H(z) = K$ produces the closed-loop characteristic equation:

$$z^2 + \left[\frac{K}{k^*}A - 2e^{-aT}(cosbT)\right]z + \left[\frac{K}{k^*}B + e^{-2aT}\right] = 0 \tag{6.12}$$

To set the modulus of the roots equal to unity, we set the last term to unity, or, with substitution of the definition of B,

$$\frac{K}{k^*}\left(e^{-aT} + \frac{a}{b}e^{-aT}sinbT - e^{aT}cosbT\right) + e^{-2aT} = 1 \tag{6.13}$$

Roots may be found analytically and plotted versus various parameters. In Figure 6.7 we show the dependence of b on the sampling period T, along with the dependence of the stabilizing damping

Parameter Values for Figure 6.7

Parameter		Value	Units
m	=	0.30	kg
k	=	5000	N/m
m*	=	0.02	kg
b*	=	3.75	N/m/s
k*	=	257	N/m

coefficient in the uncoupled case, from Figure 6.2. Particular values have been chosen for each of the parameters, including the parameters for the assumed human impedance for this plot, as shown in Table 6.3.2. Note that the positive damping b^* contributed by the human impedance provides for the possibilty of adding negative damping for low sampling periods.

Unfortunately, these data do not lend themselves to presentation in non-dimensionalized variables.

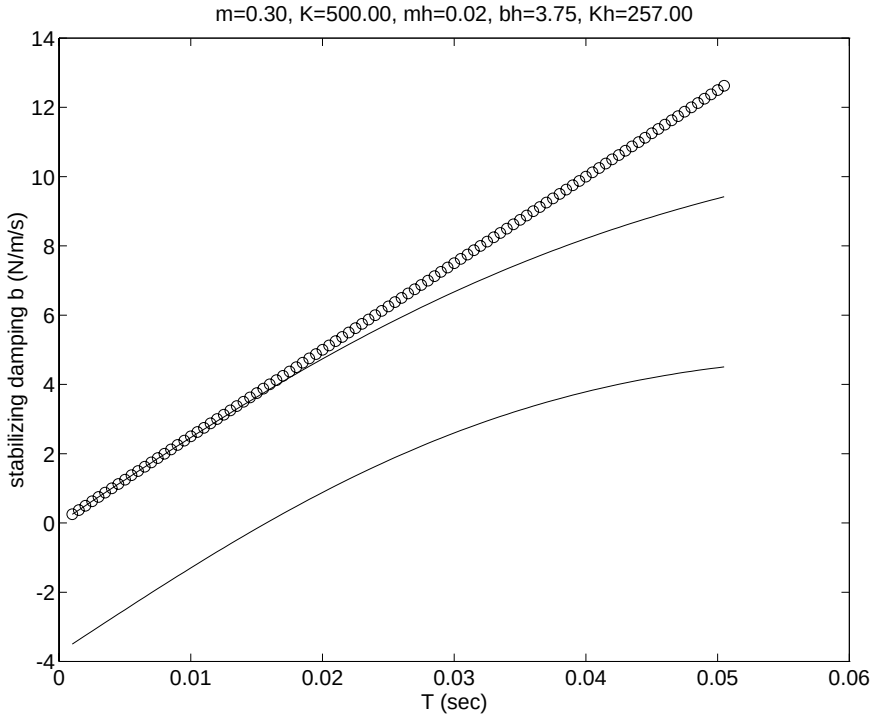

Figure 6.7: *Stabilizing Damping versus Sampling Period*

6.4 Effects of the intersample threshold crossing

In this section, we will evaluate the negative impacts of the intersample threshold crossing upon the stability of a virtual wall-rendering manipulandum coupled to a particular human. From Chapter 5, we have a controller design in hand which, with deadbeat control techniques, is able to eliminate the effects of intersample threshold crossing, even while working within the constraints of a sampled data controller. But before we bother to implement this special control technique, we would like to know what we will be gaining and thus undertake a bit of analysis of a controller which does not use this technique. We will be treating the destabilizing effects of the intersample threshold crossing (ITC) independently of the zero order hold (ZOH) and will thus produce a separate stabilizing damping coefficient. An appropriate use for this ITC-effect balancing damper would be as a safety margin in damping to add to a system which uses ZOH compensation but not ITC compensation.

In order to treat ITC independently of the ZOH, we will set up the following system for analysis: a continuous but switching controller (two modes) in which the switching times must fall on integer multiples of a fixed sampling period T.

$$t_{on},\, t_{off} \,\epsilon\, \{jT \,|\, j \epsilon \mathcal{Z}\} \tag{6.14}$$

The first detection of a position beyond the switching line, occurring on a sampling time, will trigger a switch. Thus the latency in switching can last up to one full sample period T. Once the switch has been thrown, the controller operates like an analog controller, without sampling and without a zero-order held controller output.

Standard laws of conservation of energy do not apply to time-varying systems. For example, discontinuously increasing the stiffness of a compressed spring will all of a sudden increase that spring's stored energy. The kinetic energy of a moving mass will abruptly increase at time t if the mass increases at time t. Discontinuously changing the stiffness of an uncompressed spring, or the mass of an unmoving object, however, cannot add energy. This fact has been used to advantage in the design of physical models for sound synthesis by Van Duyne and Pierce [99]. An evolving spectrum can be effected in a physically modeled string by using a nonlinear spring for the model of the bridge. If the spring discontinuously changes spring constants, but does so only when unextended, it will cause the spectral energy to rise in frequency without affecting the damping characteristics. Evolving spectra are characteristic of some musical instruments, for example the gong. Van Duyne and Pierce call such model components 'passive nonlinearities'.

Our system contains an element which would have been considered a passive nonlinearity, had it not been for the latency in switching times. Nominally, (if switching times were *on* threshold

crossings), the system could not gain energy since the switching would, in that case, occur when the spring of the virtual wall is uncompressed.

Since we cannot implement our would-be passive nonlinearity in a sampled data setting, we now ask the following questions:

First, if energy is introduced by switching on a spring in a compressed state (as takes place at wall entrance), and energy is extracted by only first turning off the spring in a stretched state (at wall exit), can we say that the energy introduced is balanced by the energy extracted? Or do there exist pathological cases in which the net energy continually increases, resulting in unbounded growth of the state variables?

Second, under a worst case assumption, where maximum energy is introduced for every wall strike, what damping coefficient must be included in our system to guarantee stability? When the manipulandum strikes the wall (the threshold is crossed) just at that time between sampling times which makes for the worst latency, what is the largest discontinuous jump in potential energy in the spring?

To answer these questions, we make use of Poincaré maps. Poincaré maps (also called return maps) are often used in the field of nonlinear dynamics to treat discontinuous (switching) systems. By expressing the dynamics of a switching system in a return map, the switching dynamic effectively disappears. The switching analog system is transformed into a non-switching discrete system. As a time-invariant discrete system model, the return map lends itself to analysis by standard tools from linear discrete systems theory.

To develop a full appreciation for the complexity of our system, especially to point out that the net amount of energy introduced (or extracted) is a function of both the time and the state at each strike, I first present a full return map, without simplifying assumptions. Thereafter, section 6.4.4 will present a simplified map and its associated assumptions. The full return map will only be useful for numerical studies, whereas the one-dimensional map will lend itself to analytical treatment.

6.4.1 Full return map

To formulate a return map, we choose the Poincaré section at $y = 0$ (the wall threshold) and further choose, from the two crossings per bounce, only the crossing of this section in the positive y direction (the wall exit). Thus our return map will be a composite of two maps: F_1, which maps the system state from wall exit to wall entry, and F_2 which maps the system state from wall entry to the next wall exit.

$$F = F_1 \circ F_2 \tag{6.15}$$

Figure 6.8 defines the time points and time intervals which will enter into our discussion during

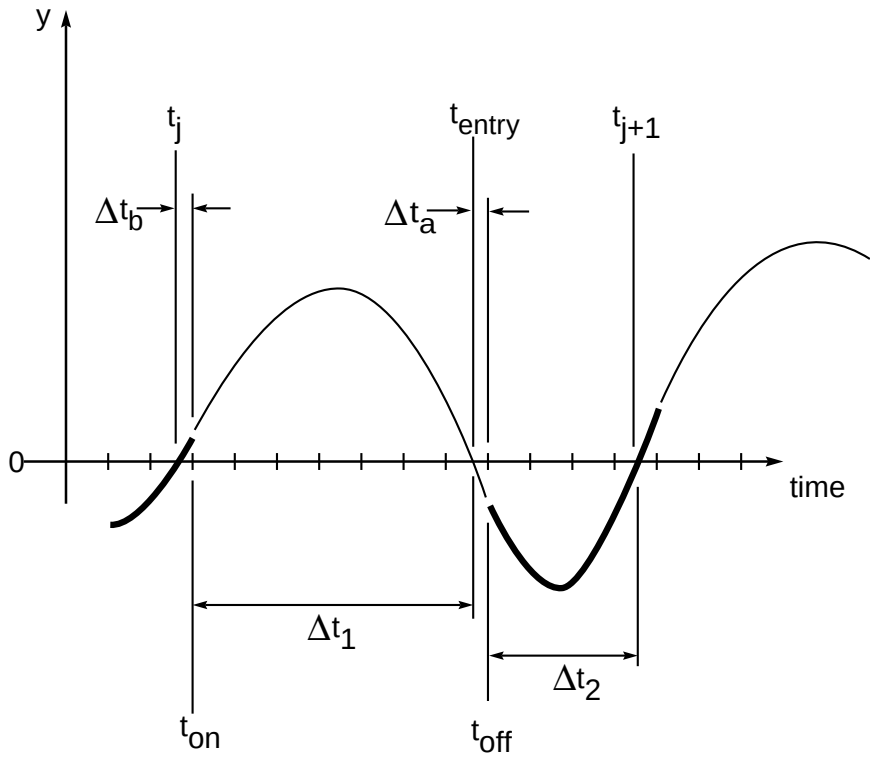

Figure 6.8: *Sampling Points in a Typical floor Strike*

the construction of F_1 and F_2. Note that the map F_1 and F_2 shall both express evolution according to the *wall off* and *wall on* models, because of the asynchrony between threshold crossings and switching times and our choice of the threshold as the Poincaré section. Primarily, however, F_1 expresses evolution under the *wall on* and F_2 expresses evolution under the *wall off* model.

We shall only need to carry two variables to characterize the switching sequence, namely t_j and v_j, since the position y_j is zero at each threshold crossing (the chosen Poincaré section). Thus the map F is made up of two functions f and g:

$$F : \begin{cases} t_{j+1} = f(t_j, v_j) \\ v_{j+1} = g(t_j, v_j) \end{cases} \tag{6.16}$$

To be fully explicit, we show F_1 and F_2 cast in the same form below.

$$F_1 : \begin{cases} t_{entry} = f_1(t_j, v_j) \\ v_{entry} = g_1(t_j, v_j) \end{cases} \tag{6.17}$$

$$F_2 : \begin{cases} t_{j+1} = t_{exit} = f_2(t_{entry}, v_{entry}) \\ v_{j+1} = v_{exit} = g_2(t_{entry}, v_{entry}) \end{cases} \tag{6.18}$$

Two models will govern the motion of the ball, the ball being our model of the manipulandum under the finger or hand of the human. One will govern during the *wall on* periods of motion, to be known as Model I, and another will govern during the *wall off* periods, known as Model II. Various model types may be used for Model I (including a ball falling freely or with damping in a gravity field or a lightly-sprung mass with or without damping and gravity), so long as the ball, moving according to such model, will return to the wall in finite time. Note that the gravity field represents a constant bias force from the hand of the human operator. Model II will generally take the form of a sprung mass, with or without damping and gravity, wherein the spring represents the virtual wall stiffness. The following development will assume that explicit solutions exist to both Model I and Model II. But before assuming particular models, I will construct the full return map F without reference to particular models. Models will be assumed just before introducing the numerical studies.

We will require the following four functions, constructed from the solutions of Model I and Model II.

First, function $y_i : \Re^2 \times \Re \to \Re^2$ returns the state x, (where $x = [y, v]'$) which results from evolution according to Model I from the initial condition x_0:

$$\mathbf{x} = y_i(\mathbf{x_0}, t) \tag{6.19}$$

Second, we will require a function $t_i : \Re^2 \to \Re$ which returns the time remaining to wall strike employing Model I given an initial condition:

$$\Delta t_1 = t_i(\mathbf{x_0}) \tag{6.20}$$

Third, function $y_{ii} : \Re^2 \times \Re \to \Re^2$ is used to evolve the state according to Model II:

$$\mathbf{x} = y_{ii}(\mathbf{x_0}, t) \tag{6.21}$$

Finally, a function $t_{ii} : \Re^2 \to \Re$ will return the time remaining to wall strike employing Model II given an initial condition:

$$\Delta t_2 = t_{ii}(\mathbf{x_0}) \tag{6.22}$$

We begin with the construction of F_1.

Although the ball has just passed the threshold, exiting the wall at t_j, it continues to travel according to Model II (*wall on*) to the end of the sample period containing t_j. The time t_{off} at which Model I takes over from Model II is given by:

$$t_{off} = T(1 + floor\left[\frac{t_j}{T}\right]) \tag{6.23}$$

where the *floor[]* function returns the largest integer less than its argument.

We use Model II to evolve the state from $x_j = [0, v_j]'$ at t_j to x_{off} at t_{off}.

$$x_{off} = y_{ii}(x_j, t_{off} - t_j) \tag{6.24}$$

The time to wall strike is found from the state x_{off} using function t_i:

$$\Delta t_1 = t_i(\mathbf{x_j}) \tag{6.25}$$

We already have the two components of F_1, f_1 and g_1:

$$\begin{cases} t_{entry} = t_{off} + \Delta t_1 \\ x_{entry} = y_i(\mathbf{x}_{off}, \Delta t_1) \end{cases} \tag{6.26}$$

The position component of x_{entry} will be zero, only v_{entry} is required for the map.

Now for the construction of F_2.

The time at which Model II takes over from Model I, t_{on} occurs on the first sampling time after t_{entry}, and is found with:

$$t_{on} = T(1 + floor\left[\frac{t_{entry}}{T}\right]) \tag{6.27}$$

The state at t_{on} is available using function y_i:

$$x_{on} = y_i(x_{entry}, t_{on} - t_{entry}) \tag{6.28}$$

To bring the state to time $t_{j+1} = t_{exit}$, we require the time spent in Model II:

$$\Delta t_2 = t_{ii}(x_{on}) \tag{6.29}$$

We now may express the time and state at t_{j+1}:

$$\begin{cases} t_{j+1} = t_{on} + \Delta t_2 \\ x_{j+1} = y_{ii}(x_{on}, \Delta t_2) \end{cases} \tag{6.30}$$

The position y_{j+1} will be zero. The threshold crossing sequence requires only v_j and t_j.

6.4.2 Substitution of models

Unfortunately, the full return map does not yield itself to further analysis since it includes the non-analytic floor function. The floor function serves to place the switching times properly on the sampling times, always choosing the next sampling time after a threshold crossing. But the presence of the floor function is not the only property which makes this map difficult to analyze. The other property is the coupling between the two component functions f and g. The latency in switching between models has an effect on the ensuing threshold crossing velocity. Thus the exit velocity v_{j+1} is a function (denoted g) of both t_j and v_j. Likewise, the time period for which the ball remains in the wall is a function of the velocity at wall strike, and thus t_{j+1} is a function (denoted f) of v_j as well as t_j. Thus we have a two-dimensional map, for which far fewer tools are available than for one-dimensional maps.

The utility of this full return map lies in efficient numerical studies. To demonstrate one such numerical study, and thereby further highlight the interesting complexity of our system, I will assume two simple undamped models for Model I and Model II and use them to run numerical simulations.

Model I will take the form of a ball falling freely in a gravity field. Function y_i (Equation 6.19) thus reads:

$$\begin{aligned} y &= v_0 t - \tfrac{1}{2} g t^2 \\ v &= v_0 - g t \end{aligned} \tag{6.31}$$

Function t_i (Equation 6.20) using the freely falling ball model reads:

$$\Delta t_1 = \frac{-v_0 + \sqrt{v_0^2 + 2 g y_0}}{g} \tag{6.32}$$

Function y_{ii} (Equation 6.21) using a model of a sprung mass without damping reads:

$$\begin{aligned} y &= A cos\omega t + B sin\omega t - g/\omega^2 \\ v &= -(\omega y_0 + g/\omega) sin\omega t | v_0 cos\omega t \end{aligned} \tag{6.33}$$

where $\omega = \sqrt{k/m}$, $A = (y_0 + g/\omega^2)$ and $B = v_0/\omega$.

Finally, the function t_{ii} (Equation 6.22) reads:

$$\Delta t_2 = \frac{1}{\omega}\left[\pi + atan2(A, -B) + asin\left(\frac{g/\omega^2}{\sqrt{A^2+B^2}}\right)\right] \tag{6.34}$$

The return map defined above, used with these function definitions, yields a very efficient means of computing the sequence of threshold crossings.

The map is simply too complicated to make any analytical deductions regarding the balance of energy gain with energy loss. However, we may use it to conduct numerical studies into these questions. Intuitively, we may expect that as the samping period decreases, the amount of energy gained because of intersample threshold crossing will decrease. We have tested this hypothesis as follows. The map was used to compute the exit velocity for 40 strikes of the wall, using various sampling periods. The maximum strike velocity of those 40 is ploted versus the sampling period in Figure 6.9 The sampling period was varied in increments of .0001 from 0.01 to 0.3 seconds.

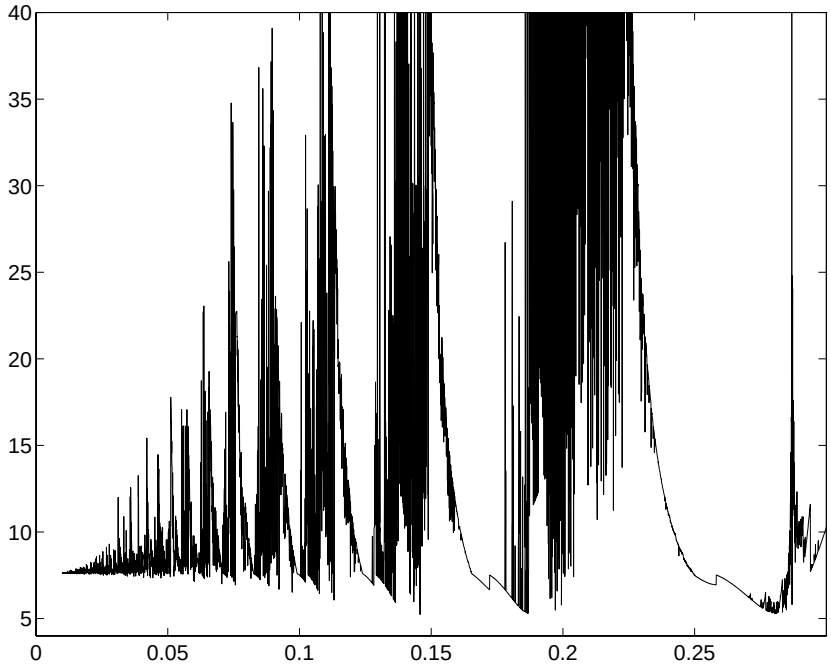

Figure 6.9: *Maximum exit velocity of 40 strikes versus sampling period*

We observe that the maximum velocity attained does seem to decrease with decreasing sampling

period. But perhaps more interesting is just how non-predicatable the situation really is.

6.4.3 Simulations and Checks on the Return Map

I will briefly describe the manner in which we have verified the return map against simulations and evaluations of model solutions. This section will provide a transition to the next, in which simplifying assumptions render the return map analytically tractable.

Model simulations may be run according to algorithms which account for the sampled data implementation such as those introduced in Chapter 5. Alternatively, since we have assumed models which posess solutions, it is only necessary to evaulate the solutions according to an appropriate switching algorithm to produce time histories of the system. As a further check, we have found expressions for the kinetic energy, potential energy and dissipated energy as a function of state and history for various models. Highlighting our verification procedure here, and taking this opportunity to present plots of the kinetic, potential, and dissipated energy will further exemplify the coupled and complex nature of this nonlinear system.

Figure 6.10a) shows the Kinetic Energy KE, Potential Energy PE and cumulative dissipated energy E_d in a time chart above the position and velocity trajectories of Figure 6.10b). These plots pertain to the full sampled data simulation containing the $floor$ function. Note that the potential energy (stored in the spring and gravity field) jump discontinuously at wall entry and exit. Energy is gained at wall entry and lost at wall exit, to differing degrees. The energy dissipated may never catch up to the total energy. The ball may not stop bouncing, despite the presence of dissipation in this model.

By contrast, Figure 6.11 shows the state evolution and energy evolution in the case where the switching times are *on* the threshold crossings. In this figure, which corresponds to *physical* behavior, or the successful implementation of a passive nonlinearity, we see that the total Energy is conserved.

We now turn to an analysis of worst-case scenarios.

Figure 6.12 shows the energy and state evolution of the worst-case system without bias with the balancing damping b_{bal}.

A phase-plot of the worst-case scenario is also informative as in Figure 6.13. The growth in state due to delayed switching can be clearly seen. Delayed switching across the threshold (switching in the first quadrant at wall exit and in the third for wall entry) causes the state trajectory to jump onto paths which are further and further from the origin.

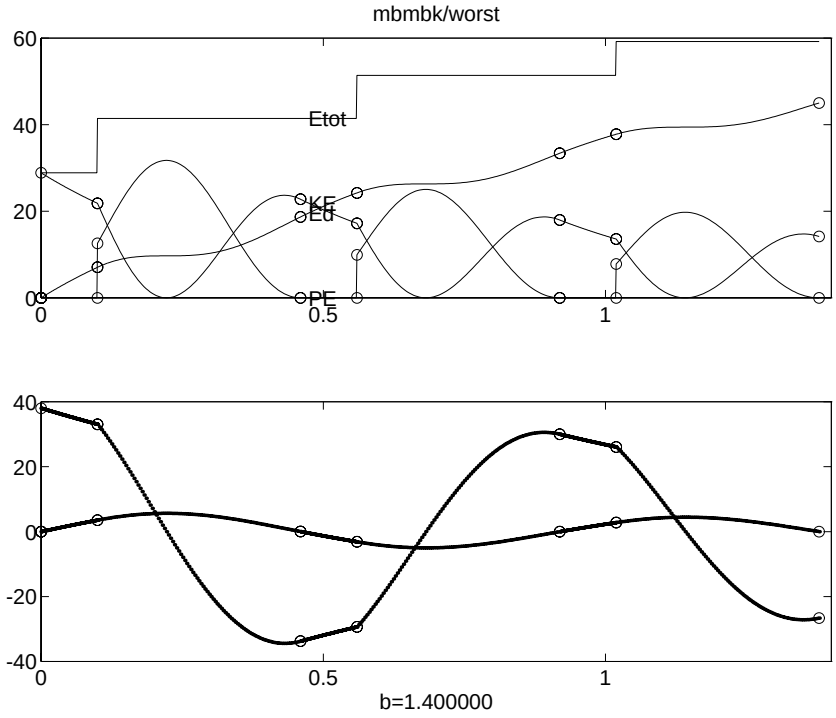

Figure 6.10: *Floored*

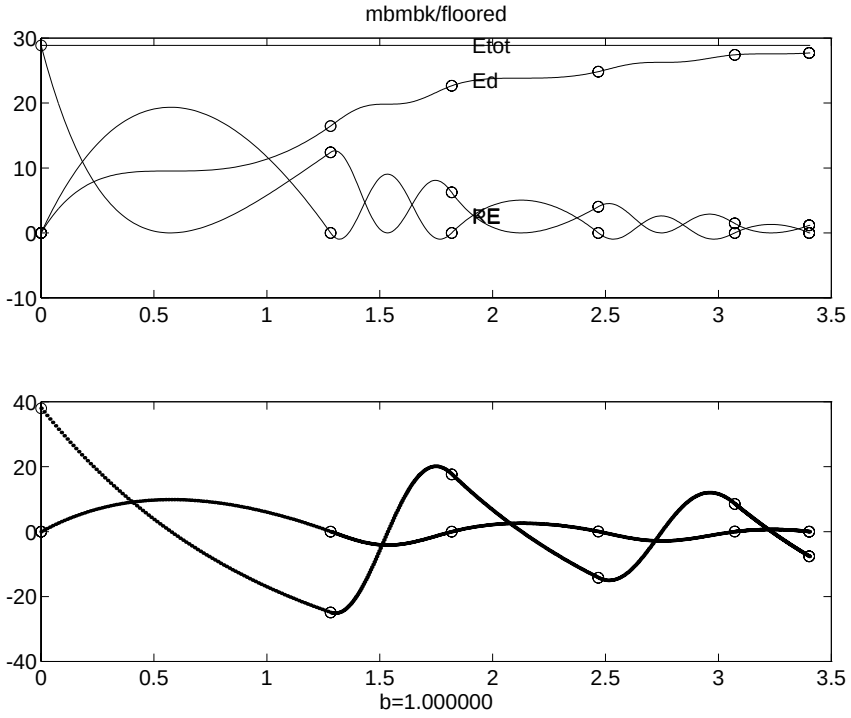

Figure 6.11: *Physical*

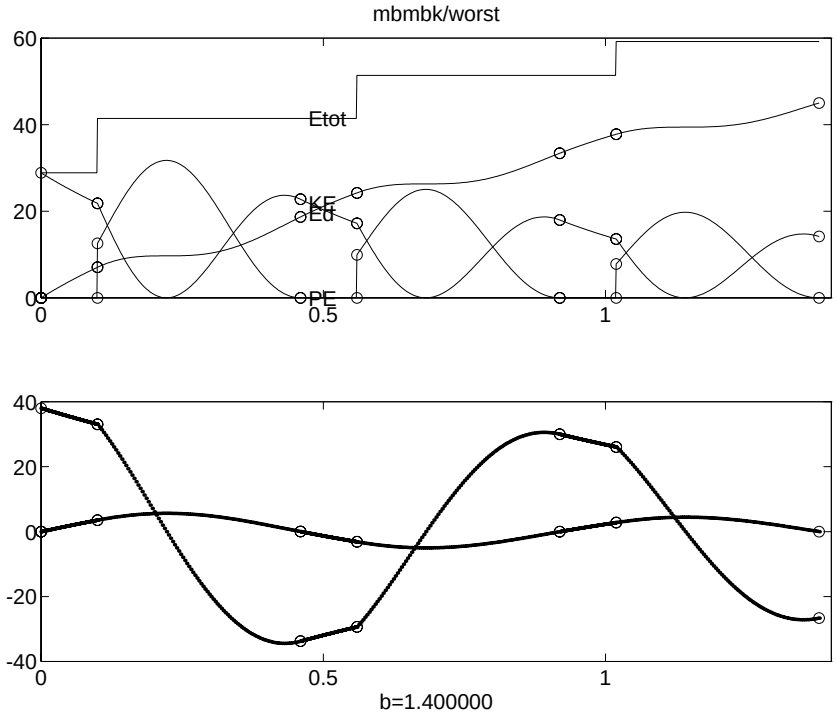

Figure 6.12: *Worst-Case*

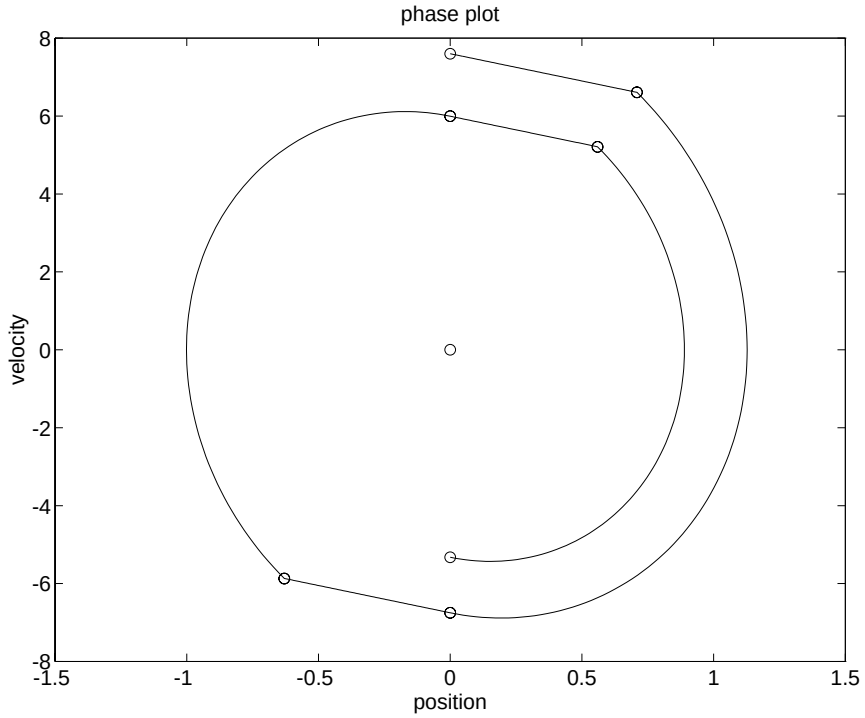

Figure 6.13: *Worst-Case Phase Plot*

6.4.4 Effects of intersample threshold crossing under worst-case assumptions and non-existent bias force

The worst case energy gain obtains when our bouncing ball hits the wall (crosses the threshold) immediately after a sampling time. In this manner, the ball will pierce the wall to a maximum depth while traveling according to Model I —using an entire sampling period. The minimum energy loss obtains when the ball is held back by the spring of the wall upon exit for minimum time. Thus the wall turn-on switching time occurs T seconds after wall entry and the wall turn-off switch occurs right on wall exit in the worst-case scenario.

Under this worst case assumption we may seek the damping coefficient b which will dissipate the energy gained. This is of course a much simpler problem than that of the previous section, where the $floor$ function was involved. In the present case, if the strike velocity is the same from one wall encounter to the next (as will be the case when the balancing damping b_{bal} has been found), then the energy gain will be the same from one encounter to the next. This was not the case in the full return map because the energy gained at each bounce had to do with both the strike time and strike velocity.

The balancing damping coefficient, however, still may not be found analytically until we make one further assumption. Unfortunately, no analytical solutions exist to the following deceptively simple equation:

$$e^{a\theta}cos(\theta) = C \tag{6.35}$$

The roots of this equation are the intersection of a logarithmic spiral with an off-axis vertical line. Its solution is necessary to express the time to exit the wall given the wall entry velocity. The constant on the right-hand-side arises from the non-zero bias force of gravity bearing down. In full form, we seek the time Δt_2 which solves the following equation:

$$y(\Delta t_2) = e^{a\Delta t_2}(Acos\omega\Delta t_2 + Bsin\omega\Delta t_2) - g/\omega_0^2 = 0. \tag{6.36}$$

Beyond a certain time, the curve of an exponential spiral will no longer intersect an off-center line. Thus the solution we seek is not a periodic function.

We therefore make one more simplifying assumption. We set the bias force to zero ($g = 0$) and further, to ensure that the ball will return to the wall in finite time, we use a sprung mass for Model I. We set the spring constant on Model I, K_1, much lower than that on Model II, retaining the wall switching characteristic.

We may now treat our problem analytically, developing the map as follows:

Function y_i, which expresses evolution of Model I (Equation 6.19) takes the form:

$$\begin{aligned} y_1(t) &= e^{-\sigma t}(A_1 cos w_1 t + B_1 sin w_1 t) \\ v_1(t) &= e^{-\sigma t}\left[(B_1 w_1 - A_1\sigma)cos\omega_1 t - (B_1\sigma + A_1\omega)sin w_1 t\right] \end{aligned} \tag{6.37}$$

The initial conditions are used to define A and B:

$$\begin{aligned} y_1(0) = y_{10} = 0 \Rightarrow A_1 = 0 \\ v_1(0) = v_{10} \Rightarrow B_1 = v_{10}/\omega_1 \end{aligned} \tag{6.38}$$

The time spent in Model I (function t_i, Equation 6.20) is given simply as:

$$\Delta t_1 = \pi/\omega_1 \tag{6.39}$$

The function y_{ii} (Equation 6.21) is similar to function y_{ii}, but with a larger spring stiffness K_2, and thus larger natural frequency ω_2:

$$\begin{aligned} y_2(t) &= e^{-\sigma t}(A_2 cos w_2 t + B_2 sin w_2 t) \\ v_2(t) &= e^{-\sigma t}\left[(B_2 w_1 - A_2\sigma)cos\omega_2 t - (B_2\sigma + A_2\omega)sin w_2 t\right] \end{aligned} \tag{6.40}$$

Constants A_2 and B_2 are evaluated using the initial conditions:

$$\begin{aligned} y_2(0) = y_{20} \Rightarrow A_2 = y_{20} \\ \dot{y}_2(0) = v_{20} \Rightarrow B_2 = v_{20}/\omega_2 \end{aligned} \tag{6.41}$$

The time spent in model II is handled by function t_{ii} (Equation 6.22), defined as follows:

$$\Delta t_2 = (1/\omega_2)atan2(-A_2, B_2) \tag{6.42}$$

With the functions y_i, t_i, y_{ii}, and t_{ii} in hand, we may develop an explicit expression for the return map in a manner similar to the development of the full return map above.

The time spent in Model I is simply one sampling period added onto the time spent outside the wall:

$$\Delta t_1 = \pi/\omega_1 + T \tag{6.43}$$

The state at wall entry may then be found using Δt_1 in Equation 6.37

$$\begin{aligned} y_{20} = y_1(\Delta t_1) &= e^{-\sigma\Delta t_1}\tfrac{v_{10}}{\omega_1} sin(\omega_1\Delta t_1) \\ v_{20} = v_1(\Delta t_1) &= e^{\sigma\Delta t_1}\left[v_{10}cos(\omega_1\Delta t_1) - \tfrac{v_{10}}{\omega_1}\sigma sin(\omega_1\Delta t_1)\right] \end{aligned} \tag{6.44}$$

The time spent inside the wall is given by:

$$\Delta t_2 = \frac{1}{\omega_2} tan^{-1}\left(\frac{-A_2}{B_2}\right) = \frac{1}{\omega_2} tan^{-1}\left(\frac{-y_{20}}{(1/\omega_2)(v_{20} + y_{20}\sigma)}\right) \tag{6.45}$$

After substituting for y_{20} and v_{20} from equation 6.44, this equation simplifies to:

$$\Delta t_2 = \frac{1}{\omega_2} tan^{-1}\left(\frac{\omega_2}{\omega_1} tan(\omega_1 t_1)\right) \tag{6.46}$$

We have, since Δt_2 is the time to wall threshold,

$$y_2(\Delta t_2) = e^{-\sigma \Delta t_2}\left[A_2 cos\omega_2 \Delta t_2 + B_2 sin\omega_2 \Delta t_2\right] = 0 \tag{6.47}$$

The velocity at wall exit is expressed using Δt_2 in Equation 6.40:

$$v_2(\Delta t_2) = e^{-\sigma t_2}\left[(B_2 w_1 - A_2\sigma)cos\omega_2 t_2 - (B_2\sigma + A_2\omega)sinw_2 t_2\right] \tag{6.48}$$

re-arranging, we have:

$$v_2(\Delta t_2) = e^{-\sigma t_2}\left[-\sigma(A_2 cos\omega_2 t_2 + B_2 sin\omega_2 t_2) + \omega_2(B_2 cos\omega_2 t_2 - A_2 sin\omega_2 t_2)\right] \tag{6.49}$$

but, from Equation 6.47, the first term is zero. So

$$v_2(\Delta t_2) = e^{-\sigma t_2}\omega_2\left(B_2 cos\omega_2 t_2 - A_2 sin\omega_2 t_2\right) \tag{6.50}$$

$$= e^{-\sigma t_2}\omega_2\left(\frac{1}{\omega_2} e^{-\sigma t_1} v_{10} cos(\omega_1 t_1) cos\omega_2 t_2) - e^{-\sigma t_1}\frac{v_1 0}{\omega_1} sin(\omega_1 t_1 sin(\omega_2 t_2)\right) \tag{6.51}$$

$$= e^{-\sigma(t_1+t_2)} v_{10}\left(cos(\omega_1 t_1) cos(\omega_2 t_2) - \frac{\omega_1}{\omega_2} sin(\omega_1 t_1) sin(\omega_2 t_2)\right) \tag{6.52}$$

The return map may now be expressed as follows:

$$\begin{aligned} t_{j+1} &= t_j + \Delta t_1 + t_1 + t_2 \\ v_{j+1} &= e^{-\sigma(t_1+t_2)} v_j\left[cos\omega_1 t_1 cos\omega_2 t_2 - \tfrac{\omega_2}{\omega_1} sin\omega_1 t_1 sin\omega_2 t_2\right] \end{aligned} \tag{6.53}$$

where

$$\begin{aligned} t_1 &= \tfrac{\pi}{\omega_1} + T \\ t_2 &= \tfrac{1}{\omega_2} tan^{-1}\left(\tfrac{\omega_1}{\omega_2} tan\omega_1 t_1\right) \end{aligned} \tag{6.54}$$

Note that our two functions f and g are decoupled:

$$\begin{cases} t_{j+1} = f(t_j) \\ v_{j+1} = g(v_j) \end{cases} \tag{6.55}$$

We may find the Jacobian of the map

$$J = \begin{bmatrix} \frac{\partial f}{\partial t} & \frac{\partial f}{\partial v} \\ \frac{\partial g}{\partial t} & \frac{\partial g}{\partial v} \end{bmatrix} = \begin{bmatrix} 1 & 0 \\ 0 & e^{-\sigma(t_1+t_2)} \left(cos(\omega_1 t_1) cos(\omega_2 t_2) - \frac{\omega_1}{\omega_2} sin(\omega_1 t_1) sin(\omega_2 t_2) \right) \end{bmatrix} \tag{6.56}$$

Setting the determinant of the Jacobian equal to 1, we find the limit cycles (fixed points) are given by:

$$\sigma = \frac{1}{t_1 + t_2} ln \left(cos(\omega_1 t_1) cos(\omega_2 t_2) - \frac{\omega_1}{\omega_2} sin(\omega_1 t_1) sin(\omega_2 t_2) \right) \tag{6.57}$$

This equation may be solved numerically for b_{bal}, the balancing damping coefficient.

Figure 6.14 shows the balancing b_{bal} as a function of the period T under the worst case assumpion.

As mentioned above, solutions are not available when $g \neq 0$, but they may still be found numerically. Having a semi-analytic result in hand for the case $g = 0$ allows us to proceed with a bit more confidence.

Figure 6.15 shows a three-dimensional plot with the analytical solution highlighted. The bias force (gravity) increases and is seen to have a increasing influence on the damping coefficient b, but not as strong as the sampling period T. (Within the range shown).

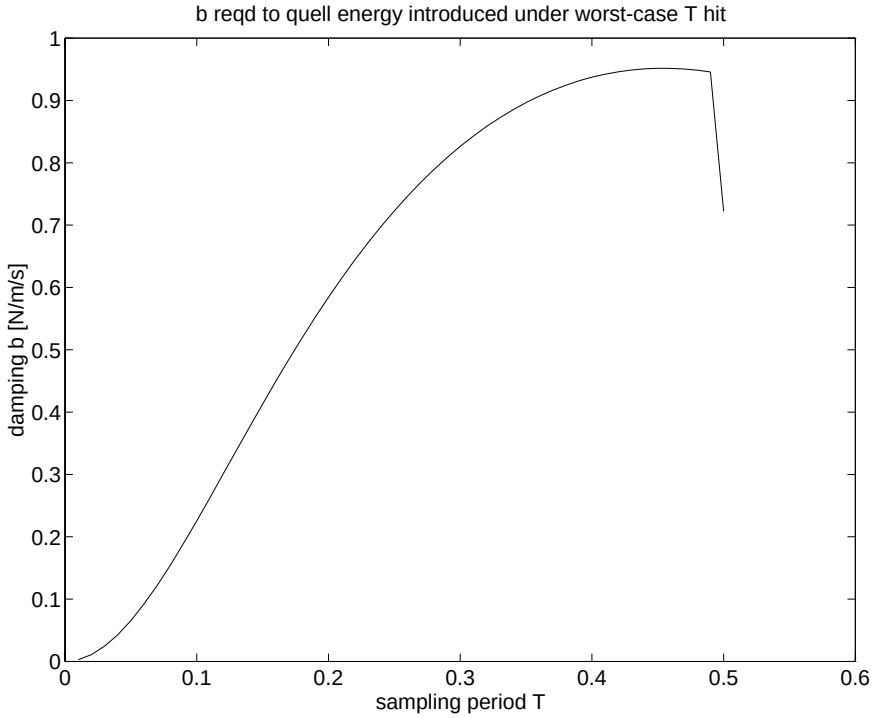

Figure 6.14: *Damping required to quell the energy introduced under worst-case assumptions*

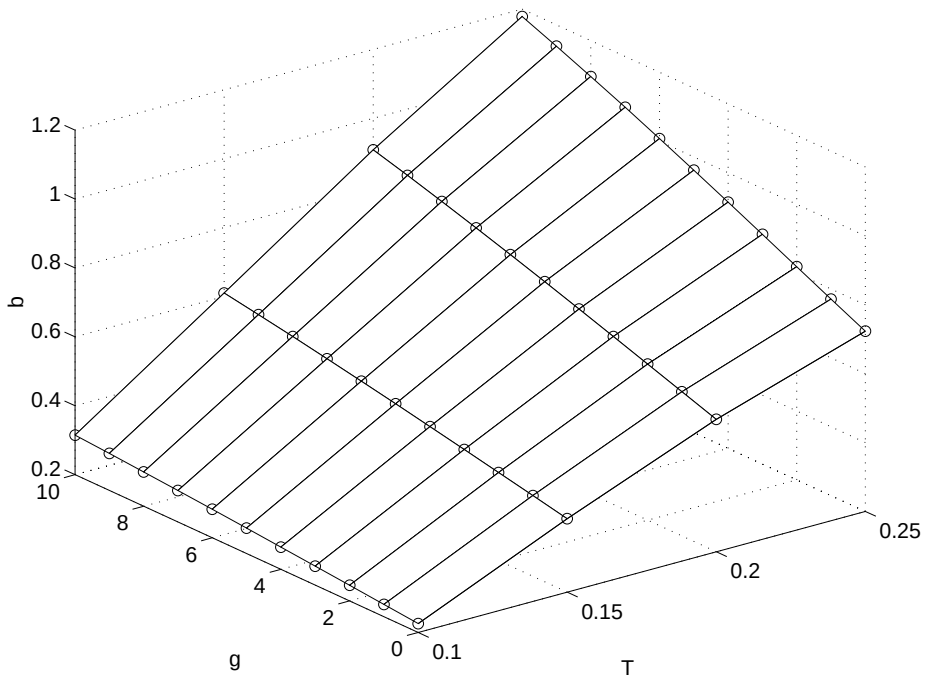

Figure 6.15: *Stabilizing damping as a function of both samping period T and bias force g*

6.5 Summary

In this chapter, measures for the destabilizing effects of the zero order hold and the intersample threshold crossing have been found which are useful in determining the worthiness for implementation of the control techniques introduced in the previous chapter. An analytical solution for the damping coefficient which will balance the destabilizing effects of intersample threshold crossing under worst-case and non-existant bias force from the human was presented. Numerical extensions of this result were made with a Poincaré map.